Journal of The Electrochemical Society

OPEN ACCESS

Dynamic Surface Stress Response during Reversible Mg Electrodeposition and Stripping

Dynamic Surface Stress Response during Reversible Mg Electrodeposition and Stripping

Yeyoung Ha,[a] Zhenhua Zeng,[b,*] Christopher J. Barile,[a] Jinho Chang,[a] Ralph G. Nuzzo,[a] Jeffrey Greeley,[b,*,z] and Andrew A. Gewirth[a,,z]**

[a]*Department of Chemistry, University of Illinois, Urbana, Illinois 61801, USA*
[b]*School of Chemical Engineering, Purdue University, West Lafayette, Indiana 47907, USA*

Through the use of in situ electrochemical surface stress measurements, Mg deposition and stripping processes in electrolytes for Mg batteries are studied. We examine four electrolytes: PhMgCl+$AlCl_3$/THF, (DTBP)MgCl–$MgCl_2$/THF, $MgCl_2$+$AlCl_3$/THF, and $Mg(BH_4)_2$+$LiBH_4$/diglyme. Each of these electrolytes exhibits common surface stress response features, indicating that the mechanisms of Mg deposition and stripping are similar among the different electrolytes. Combining the measurements with density functional theory calculations, each part of the stress-potential curve is assigned to steps in the deposition and stripping reactions. The analysis suggests the following mechanism: (1) Mg^{2+}/anion/solvent complexes adsorb on the substrate prior to the deposition; (2) Mg deposits as random nuclei and the deposition continues without a recrystallization process; (3) during the initial stage of Mg stripping, less coordinated Mg(0) is converted to soluble Mg(II) species and to partially oxidized species, MgO_x; (4) as the anodic reactions proceed further, Mg continues to dissolve and MgO_x is removed via chemical processes; (5) due to the strong interaction between Mg and the noble metal substrate atoms, the Mg layer directly bound to the substrate are the last to be anodically converted (and desorb).

Manuscript submitted August 11, 2016; revised manuscript received September 15, 2016. Published October 1, 2016.

There is much interest in developing rechargeable Mg batteries due to the high theoretical volumetric capacity, abundance, and benign nature of Mg. Finding a suitable electrolyte for reversible Mg deposition and dissolution, however, is challenging due to the difficulty in producing soluble Mg^{2+} and the formation of passivation films on the electrode surface.[1–3] The first reversible Mg deposition and stripping was performed in Grignard solutions,[4–6] which suffer from low anodic stability and poor ionic conductivity. The anodic stability and the Coulombic efficiency is greatly enhanced in electrolytes based on Mg organohaloaluminate, prepared via an acid-base reaction between a MgR_2 Lewis base and an $AlCl_{3-n}R_n$ Lewis acid.[7] An inorganic magnesium aluminum chloride complex from $MgCl_2$- and $AlCl_3$-based electrolyte exhibits even higher anodic stability and a lower overpotential.[8,9] However, the corrosivity of chloride and the reactivity of Lewis acids have prompted the development of newer, less corrosive electrolytes, including $Mg(BH_4)_2$ based inorganic salts with $LiBH_4$ additive electrolytes[10,11] and all-magnesium phenolate-based electrolytes.[12] Thus, previous work illustrates that several Mg systems exhibit promise as a battery electrolyte; however, their interfacial chemistries are complicated and need to be better understood.[8–13]

Efficient electrodeposition and stripping reactions are essentials in rechargeable batteries. One of the effective in operando techniques for studying such processes is monitoring the electrochemical surface stresses developed during the deposition and dissolution of metals.[14] In situ surface stress measurements are experimentally less demanding compared to other operando techniques used for the evaluation of metal anode electrochemical dynamics, such as synchrotron X-ray analysis.[15,16] These surface stress measurements, moreover, provide information on bonding configurations present at the interfacial region, which is linked to the dynamic surface structures and adsorption and desorption processes.[14] Evolution of the surface stress during metal deposition has been extensively studied and employed in determining deposition mechanisms in both ultra-high vacuum (UHV) and electrochemical environments.[14,17–20] For example, this technique has been employed very successfully in studies of the surface stress development seen on both anodes[21–26] and cathodes[27–29] for Li-ion battery systems, suggesting its utility for extensions made to other battery systems.

In this study, we monitor the electrochemical surface stress behaviors seen during the deposition and stripping of Mg in four electrolytes for Mg batteries: PhMgCl+$AlCl_3$/THF, (DTBP)MgCl–$MgCl_2$/THF, $MgCl_2$+$AlCl_3$/THF, and $Mg(BH_4)_2$+$LiBH_4$/diglyme. The results of density functional theory calculations are integrated with the experimental data to provide more atomistic insights into the chemistry occurring at the anode-electrolyte interfacial region and the mechanisms that sustain it.

Methods

Experimental.—Magnesium chloride ($MgCl_2$, ≥ 98%), aluminum chloride ($AlCl_3$, 99.999%), 2,6-di-*tert*-butylphenol (99%), phenyl magnesium chloride (PhMgCl, 2.0 M solution in THF), ethyl magnesium chloride (EtMgCl, 2.0 M solution in THF), magnesium borohydride ($Mg(BH_4)_2$, 95%), lithium borohydride ($LiBH_4$, ≥ 95%), and diethylene glycol dimethyl ether (diglyme, anhydrous 99.5%) were purchased from Sigma-Aldrich and used without further purification unless otherwise specified. Tetrahydrofuran (THF) was obtained from a solvent purification system equipped with neutral alumina columns and dried over molecular sieves (3 Å) before use.

Electrolytes were prepared in an Ar-filled glove box, following procedures previously reported in the literature. The "all phenyl" complex (APC) was synthesized from PhMgCl (0.8 M) and $AlCl_3$ (0.4 M) in THF.[13] The magnesium aluminum chloride complex (MACC) was synthesized from $MgCl_2$ (0.06 M) and $AlCl_3$ (0.03 M) in THF.[8,9] $MgCl_2$ was dried in a tube furnace under Ar and HCl flow for 2.5 hours at 300°C as described previously.[30] The complex (DTBP)MgCl–$MgCl_2$ (0.5 M, DTBP = 2,6-di-*tert*-butylphenolate) was synthesized by reacting 2,6-di-*tert*-butylphenol with EtMgCl in THF and successively adding one equivalent of $MgCl_2$.[12] For the borohydride electrolyte, $Mg(BH_4)_2$ and $LiBH_4$ were dissolved in diglyme to give nominal concentrations of 0.1 M and 1.5 M, respectively.[10,11]

Pt cantilever working electrodes were fabricated from borosilicate glass microscope coverslips (Gold Seal No. 1, 150 μm thick) modified on one side with 20 nm of Ti followed by 150 nm of Pt, both deposited using DC magnetron sputter deposition (AJA International, Inc., Scituate, MA). Coiled Mg foil (GalliumSource, 99.95%) was used as counter and reference electrodes. A home-built electrochemical quartz cell was assembled in a glove box and sealed prior to use. The quartz cell was dried in an oven at 180°C for at least 1 hour and the Pt cantilever electrodes annealed with a H_2 flame before introduction into the glove box.

*Electrochemical Society Member.
**Electrochemical Society Fellow.
[z]E-mail: jgreeley@purdue.edu; agewirth@illinois.edu

Electrochemical measurements were performed with a 6002E Electrochemical Workstation (CH Instruments, Austin, TX), and the in situ surface stress response monitored using an optical transduction system described previously.[31,25] All potentials are reported with respect to Mg/Mg^{2+}. The cantilevers were cycled at a scan rate of 5 mV/s until a reproducible cyclic voltammogram (CV) and the corresponding surface stress responses obtained. The initial value of the surface stress at the beginning of the cathodic scan was arbitrarily set to zero, and the changes in the surface stress, Δstress, from this reference point were monitored. Refractive indexes of the solvents, 1.407 for THF and 1.408 for diglyme, were used as parameters in the stress calculations discussed below.

Computational details.—Self-consistent total energy calculations were performed based on the projected augmented wave (PAW) method[32–34] within the generalized gradient approximation (GGA-PBE),[35] as implemented in the Vienna Ab-initio Simulation Package (VASP).[36,37] Planewave basis sets with a kinetic energy cutoff of 500 eV and Monkhorst-Pack[38] k-point grids were used in the calculations. For bulk calculations of hexagonal-closed packed (hcp) Mg, face-centered cubic (fcc) MgO, and fcc Pt, Brillouin zone integration with (12 × 12 × 8), (8 × 8 × 8), and (12 × 12 × 12) k-point grids were used, respectively. The geometries were optimized until the maximum atomic forces were smaller than 0.001 eV/Å and a total energy convergence of 10^{-6} eV in the electronic self-consistent field loop was employed. The calculated Mg lattice constants are 3.215 Å and 5.121 Å for *a* and *c*, respectively, with c/a ratio of 1.59. The calculated values are comparable to the experimental results ($a = 3.21$ Å and $c = 5.21$ Å).[39] The calculated lattice constant of MgO is $a = 4.258$ Å, which is 1.1% larger than the experimentally measured value (4.212 Å).[40] Finally, the calculated Pt lattice constant is 3.977 Å and this result is 1.3% larger than the experimentally measured value of 3.924 Å.[41] All of the calculated lattice constants agree well with previous calculations using GGA-PBE.[42–44]

Mg, MgO, and Pt surfaces were modeled by repeated slabs generated with the optimized lattice constants and with at least 12 Å of vacuum perpendicular to the slab surface. Basal Mg(0001)-(2 × 2) and prismatic Mg(10$\bar{1}$0)-(2 × 1) planes were examined using (6 × 6 × 1) and (6 × 8 × 1) k-point grids, respectively, the MgO(001)-c(2 × 2) surface was calculated using (8 × 8 × 1) k-point grids, and the Pt(111)-p(2 × 2) surface was calculated using (6 × 6 × 1) k-point grids. Forces on atoms were converged to within 0.01 eV/Å, and the energy convergence criterion of 10^{-5} eV was used. Dipole corrections were employed to screen the artificial interaction through the vacuum region. Slabs with thickness ranging from 2 monolayers (ML) to 12 ML were tested. All atoms were allowed to relax so as to keep the slabs symmetric in the z-direction. For calculations with adsorbates, the bottom two layers of the slab were fixed at their optimized positions, and the remaining atoms and adsorbates were allowed to relax further.

The surface stress, σ, was calculated as previously described[45] using

$$\sigma = \frac{c}{2}\left(\frac{\tau_{XX} + \tau_{YY}}{2}\right) \quad [1]$$

where c is the supercell height in the z direction and τ_{xx} and τ_{yy} are the diagonal components of the supercell stress tensor. Excess surface stress created by adsorbates, Δσ, was calculated by

$$\Delta\sigma = \sigma^{ads} - \sigma^{clean} \quad [2]$$

where σ^{ads} and σ^{clean} are the surface stress of supercells with and without adsorbates, respectively, obtained from Equation 1. The calculated surface stress values are plotted with respect to the thickness of the slab in Å instead of ML, since the z-direction interatomic distances of Mg(0001), Mg(10$\bar{1}$0), MgO(001), and Pt(111) slabs are different.

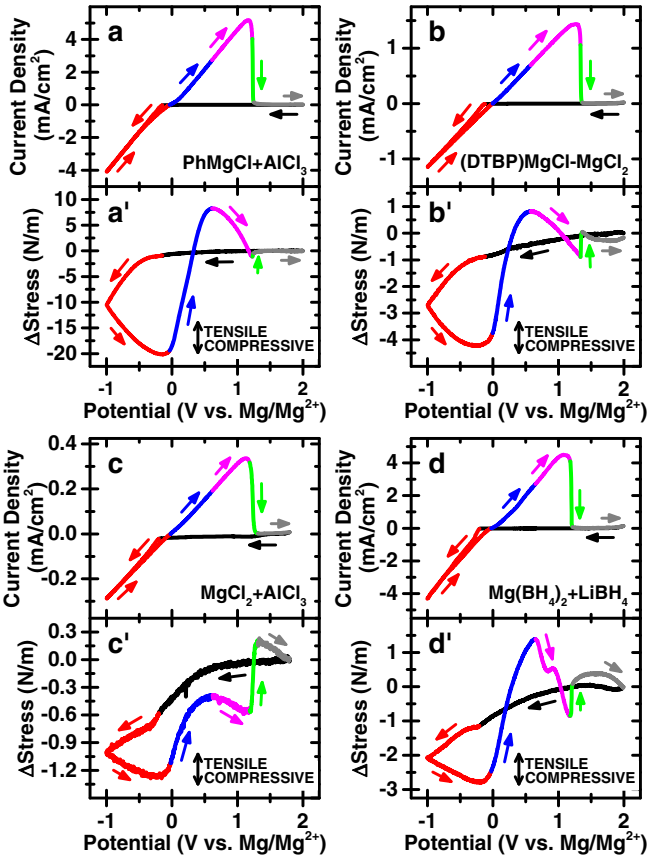

Figure 1. Cyclic voltammograms at 5 mV/s (a, b, c, and d) and corresponding surface stress responses (a′, b′, c′, and d′) during reversible Mg deposition and stripping from APC (a and a′), (DTBP)MgCl–$MgCl_2$ (b and b′), MACC (c and c′), and $Mg(BH_4)_2$+$LiBH_4$ (d and d′). Pre-deposition (black), deposition (red), initial stripping with tensile Δstress (blue), mid-stripping with compressive Δstress (magenta), last stage of stripping with a sharp tensile Δstress (green), and surface relaxation (gray) regions are color-coded for clarity.

Results

Electrochemical surface stress response.—The in situ electrochemical surface stress response was monitored during reversible Mg deposition and stripping in four different Mg battery electrolytes (Figure 1): Grignard (PhMgCl) and Lewis acid ($AlCl_3$) based APC; all-magnesium and Lewis acid-free (DTBP)MgCl–$MgCl_2$; inorganic salt ($MgCl_2$ and $AlCl_3$) solution MACC; and halide-free $Mg(BH_4)_2$+$LiBH_4$. Interestingly, the experimentally recorded surface stress responses from the four electrolytes all exhibit the same general features. First, a slight compressive Δstress is observed (black) prior to the Mg deposition. Once the Mg deposition starts, a larger compressive Δstress is observed (red), which continues in the return scan until the onset of the stripping. In the beginning of the Mg stripping, a steep tensile Δstress is observed (blue). Upon further oxidation, the surface stress response moves in a compressive direction (magenta), creating an inflection point. At the end of the stripping peak, a sharp tensile-going value of the Δstress is observed (green). The surface stress response there after relaxes to the initial value of zero (gray), with slightly different trends in the different electrolytes. The magnitude of Δstress and the amount of charge passed in each region are shown in Tables S1 and S2, respectively.

In Figure 2, Δstress values measured during the Mg deposition (red region in Figure 1) from the four electrolytes are plotted versus the deposition charge densities. The x-axis can be correlated to the equivalent Mg thickness. APC, (DTBP)MgCl–$MgCl_2$, and MACC (Figures 2a, 2b, and 2c) show a constant stress-charge density, or stress-thickness, slope during the deposition, and the magnitudes of

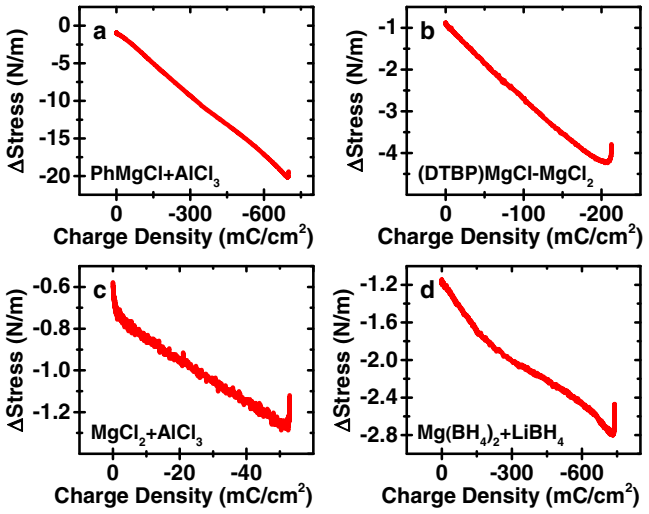

Figure 2. ΔStress during the Mg deposition from (a) APC, (b) (DTBP)MgCl–$MgCl_2$, (c) MACC, and (d) $Mg(BH_4)_2$+$LiBH_4$ plotted with respect to the deposition charge density.

the slopes are comparable. For example, the stress-charge-density slopes for APC, (DTBP)MgCl–$MgCl_2$, and MACC are all in the range of -0.22 ± 0.05 V. On the other hand, $Mg(BH_4)_2$+$LiBH_4$ (Figure 2d) shows a significantly (~5 times) smaller slope (-0.04 ± 0.01 V) as compared to those found for the other three electrolytes.

Plots of Δstress versus the charge density measured during the Mg stripping (blue and magenta regions in Figure 1) are shown in Figure 3. In all four electrolytes, the value of the measured Δstress becomes rapidly tensile at the outset of the Mg oxidation (blue), followed by a gradual compressive-going Δstress (magenta) thereafter. The magnitudes of the Δstress measured in initial (blue) and mid- (magenta) stripping regions moreover vary upon changing the negative sweep limit (Figure S1), and strong correlations between the Δstress values measured during the deposition and stripping phases are observed (Figure S2a).

In Figure 3d, two additional inflection points are present in the magenta region. The differences observed in the stress-charge density plots of $Mg(BH_4)_2$+$LiBH_4$ during deposition (Figure 2d) and stripping (Figure 3d) can be attributed to a Mg-Li alloy created in the

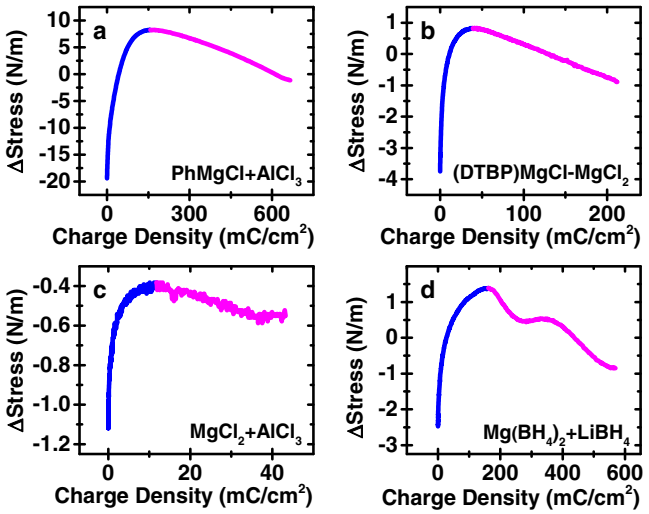

Figure 3. ΔStress during the Mg stripping in (a) APC, (b) (DTBP)MgCl–$MgCl_2$, (c) MACC, and (d) $Mg(BH_4)_2$+$LiBH_4$ plotted with respect to the stripping charge density.

Table I. Calculated surface stresses and surface energy of Mg(0001), Mg(10$\bar{1}$0), and MgO(001).

	Mg(0001)	Mg(10$\bar{1}$0)	MgO(001)
surface stress (N/m)	1.05	0.26	3.28
surface energy (J/m^2)	0.58	0.61	0.89

cathodic sweep (vide infra). Formation of a Mg-Li alloy during the Mg deposition from $Mg(BH_4)_2$+$LiBH_4$ has been previously reported.[46]

DFT calculations of the surface stress.—To further interrogate the origin of the experimentally measured surface stress changes, we performed periodic DFT calculations. The experimental results show qualitatively similar surface stress response in all four electrolytes, suggesting that neither anion nor solvent adsorption dominates the surface stress response. Therefore, we focus on materials properties of the Mg deposit. In this section, we first examine the effect of different crystal planes on the calculated surface stress. Basal Mg(0001) and prismatic Mg(10$\bar{1}$0) planes are considered since the existence of both planes in the deposited Mg film has been previously shown.[11,47] We also examine the adsorption of O on Mg, as passivation of the Mg surface due to the formation of surface oxides in Mg battery electrolytes has been previously suggested.[48,49] Finally, we evaluate the interaction between Pt and Mg.

The effect of a putative Mg-Pt alloy on the stress response can be excluded since previous XRD analyses of Mg films deposited from a Grignard-based electrolyte[47] and $Mg(BH_4)_2$+$LiBH_4$[46] electrolyte did not show any evidence of the formation of a Mg-Pt alloy (there was no shift in the Pt substrate diffraction peaks). By way of further support, we found that the surface stress response is the same on Pt, Au, and Pd cantilever electrodes (Figure S3), indicating that the surfaces stress response is not substrate dependent, but rather governed by the Mg deposition and stripping processes.

Mg(0001), Mg(10$\bar{1}$0), and MgO(001).—The calculated surface stress and surface energy of Mg(0001), Mg(10$\bar{1}$0), and MgO(001) are shown in Table I, and the optimized geometries of each slabs are shown in Figure 4. In Table I, the mean values of slabs with different thickness are presented, and the individual results are provided in Figures S4 and S5. In Figure S4, the calculated surface stress of the Mg slabs show an oscillating behavior, which can be attributed to quantum size effects.[50] Interestingly, the calculated surface stress of MgO(001) hardly oscillates. This diminished oscillation seen for the MgO(001) surface may be attributed to the lack of free electrons within the oxide, which are the source of the quantum oscillations.

The calculated surface energy of Mg(0001) plane (0.58 J/m^2) is modestly lower than that of Mg(10$\bar{1}$0) plane (0.61 J/m^2), indicating that Mg(0001) plane is slightly more stable. The same trend has been observed from previous calculations using the full charge density

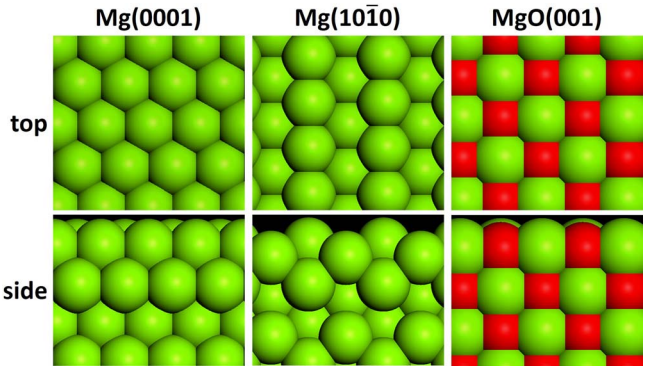

Figure 4. Top view (upper row) and side view (lower row) of optimized structures of Mg(0001), Mg(10$\bar{1}$0), and MgO(001) slabs.

Table II. Calculated excess surface stress, Δσ, and adsorption energy of Mg_{ads}, E_{ads} (vs. Mg_{bulk}), on Pt(111) and Mg(0001). Mg atom was adsorbed at fcc site on Pt(111) and hcp site on Mg(0001).

	Pt(111)	Mg(0001)
Δσ (N/m)	−0.79	−0.05
E_{ads} (eV)	−1.13	0.91

method.[51] On the other hand, the Mg(0001) plane shows a significantly more tensile surface stress (1.05 N/m) than does the Mg(10$\bar{1}$0) plane (0.26 N/m). The close surface energy values can be attributed to the existence of the same average coordination number (CN) of the surface atoms, while the difference in the surface stress can be correlated with the different atomic densities present on the surfaces. As can be seen from the top and side views of the slabs shown in Figure 4, the Mg(0001) surface is flat, and all surface atoms have the same coordination number (CN) of 9. The Mg(10$\bar{1}$0) plane, in contrast, has a corrugated surface, with a CN of 8 and 10 for the crest and trough atoms, respectively, giving an average value of 9. The intrinsic tensile surface stress on clean metal surfaces has been attributed to the redistribution of the charge of missing bonds at the surface and consequent increased bond strength between surface atoms.[52] For the Mg(10$\bar{1}$0) surface, the intrinsic tensile stress is damped significantly due to the flexibility of the surface atoms induced by corrugation. We note that a similar effect has been found in our previous calculations of structures formed by stepped Pt(221) surfaces.[45]

Comparing the surface stresses of clean Mg surfaces and that of the oxide surface, the MgO(001) surface exhibits more tensile surface stress, 3.28 N/m, than those of the clean Mg surfaces (1.05 N/m for Mg(0001) surface and 0.26 N/m for Mg(10$\bar{1}$0) surface). The larger tensile surface stress of the MgO(001) can be correlated to the stronger Mg-O binding compared to the Mg-Mg bonds on the metal surface. Indeed, the formation energy of MgO is ∼6 eV/MgO,[53] while the cohesive energy of Mg is ∼1.5 eV/Mg.[54,55]

Adsorption of Mg on Pt and Mg.—Finally, we compare the heteroatomic bonding interaction between Mg and Pt atoms to that of homometallic bonds forming between Mg atoms. The data in Table II shows the calculated excess surface stress, Δσ, of an adsorbed Mg atom, Mg_{ads}, on Pt(111) and Mg(0001) surfaces, and the corresponding adsorption energy (vs. Mg_{bulk}), E_{ads}, calculated by equation S2. Here the Mg_{ads} was placed at the most favorable sites: the fcc site on Pt(111) and the hcp site on Mg(0001), following the substrate crystal structures. Results for different slab thicknesses are shown in Figures S6 and S7, and the mean values are presented in Table II. The calculated E_{ads} indicate that the Mg-Pt interaction (−1.13 eV) is much stronger than the Mg-Mg interaction (0.91 eV). The Mg_{ads} moreover induces a greater compressive Δσ on the Pt surface as compared to that which obtained on the Mg surface.

Discussion

Pre-deposition.—Before the onset of Mg deposition (black region in Figure 1), a compressive Δstress with similar magnitude ∼−0.9 N/m (Table S1) is observed in the four electrolytes. We point out that this pre-deposition compressive Δstress is likely induced by the adsorption of Mg^{2+}/anion/solvent complexes on the surface prior to the deposition.[49,56] The comparable magnitudes of these values among the different electrolytes further suggests that qualitatively similar Mg^{2+}/anion/solvent complexes are created (albeit with different anions and solvents) and that similar coverages of these adsorbate adlayers are reached on the electrode before the deposition starts.

Deposition.—In general, the initial stage of growth, where critical nuclei form during metal deposition on an initiating substrate, creates a compressive surface stress. This is a conserved response and is found in both UHV and electrochemical environments.[19,20] The origin of this compressive stress has been attributed to the Laplace pressure exerted by the nuclei. Upon coalescence of the nuclei and formation of grain boundaries, the overall surface energy decreases and the surface stress becomes tensile. Surface stress evolution during further growth of metal film is influenced by various factors in the growth process, including grain size, growth rate, temperature, and the presence of surfactants in the electrolyte.[18-20,57–60]

During Mg electrodeposition, the present work shows that a compressive Δstress with a constant stress-thickness slope is observed (Figure 2). The absence of the tensile surface stress component here suggests that the nuclei as formed in this case do not coalesce. The island boundaries so generated are maintained throughout the deposition process and the influx of Mg atoms into them progressively elicit the development of a compressive Δstress. A less compressive Δstress per charge density during the deposition from $Mg(BH_4)_2$+$LiBH_4$ electrolyte (Figure 2d) is associated with the alloys that form in this system, which lead to the incorporation of smaller Li atoms and the formation of a less dense Mg-Li alloy. The absence of a recrystallization process[48] is likely associated with adsorption of solution species, anions and ethereal solvent molecules, at the grain boundaries. Such species will also adsorb on the freshly deposited Mg surface and relieve the intrinsic tensile surface stress of Mg surface.

Previous studies on the Mg deposition from Mg battery electrolytes suggested a random nuclei formation instead of a continuous, smooth film during the Mg electrodeposition due to a local concentration gradient of active electrolyte species.[47] Additionally, a two-stage deposition process has been proposed, where an initially porous layer is created with possible solution species trapped in the layer, following which a compact bulk deposition layer grows.[61] These reports are consistent with the development of compressive Δstress during Mg deposition. Further, a similar surface stress evolution behavior has been observed in Ni electrodeposition studies, where the tensile stress associated with island coalescence disappeared and the surface stress of Ni film became compressive in the presence of saccharin additives. In this case, the authors attribute this behavior to the inhibition of nuclei coalescence by sulfur atoms adsorbed at the grain boundaries.[62] Diffusion of adatoms into the grain boundaries has been suggested as the source of intrinsic compressive surface stresses in polycrystalline films.[63–65]

Stripping.—During the Mg stripping process, a steep tensile Δstress is observed, followed by a gradual compressive-going Δstress (Figure 3). We showed that the magnitude of the Δstress observed during the stripping of Mg depends linearly on the Δstress created during the deposition process (Figure S2a), indicating that the sources of the stripping Δstress correlate to the amount of Mg deposited on the surface. Thus, removal of Mg from the surface is a major source of the cumulative tensile Δstress observed throughout the stripping process. The presence of the inflection point and gradual relief of the tensile surface stress (magenta region), however, indicate that there are other factors that also influence the surface stress responses seen during the Mg stripping processes. Finally, the sharp tensile response (green region) seen just prior to the end of stripping is ubiquitous and indicates the presence of yet another distinct, regime-limiting stripping behavior.

In order to evaluate the origin of the aforementioned inflection point behavior, we considered stripping occurring from different Mg crystal planes. Different Mg crystal planes exhibit differential reactivity toward anodic dissolution.[66–69] In Table I, we show that the Mg(0001) surface exhibits a greater calculated tensile surface stress than that of the Mg(10$\bar{1}$0) surface. Thus, the initial sharp tensile Δstress seen on stripping likely results from preferential dissolution and/or passive oxidation response of the Mg(10$\bar{1}$0) plane, leaving the Mg(0001) plane, exhibiting a more tensile intrinsic surface stress, to comprise the majority of the active surface. As the oxidation proceeds further, Mg atoms from the less reactive Mg(0001) planes will be removed progressively and the tensile surface stress in this way relieved creates a gradual compressive-going Δstress.

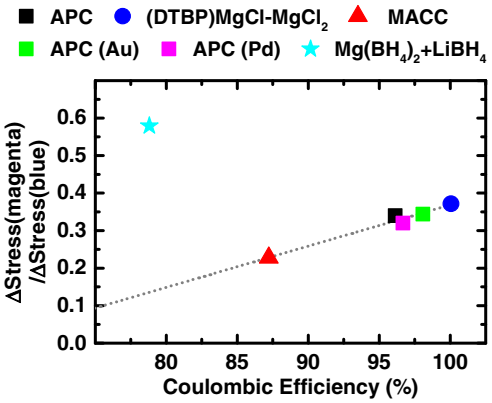

Figure 5. Relationship between the ratio of Δstress magnitude in the mid-stripping (magenta) region to that in the initial stripping (blue) region and the Coulombic efficiency. Corresponding CV and surface stress response results are shown in Figures 1 and S3.

Another origin of the inflection point behavior might be as a result of the well-known propensity of the Mg surface to create surface oxides.[70,71] It has been recently reported, for example, that sequential Mg deposition and stripping cycles led to the presence of thin residual partially oxidized species, MgO_x, whose shape and motif exemplify anisotropies in the electrolyte mediated oxidation of the (0001) and (10$\bar{1}$0) planes of Mg.[48] Our DFT calculations show that Mg oxide exhibits a more tensile surface stress than that of Mg metal (Table I). In order to analyze the effect of oxides more directly, Figure 5 reports the ratio of the Δstress magnitude in the mid-stripping (magenta) region to that in the initial stripping (blue) region versus the Coulombic efficiency. The figure shows that greater compressive-going Δstress in the mid-stripping (magenta) region is achieved at a higher Coulombic efficiency. This trend, supported by the DFT calculations, suggests that an oxygen-containing corrosion product (a passive film) is created in the beginning of the Mg stripping process (blue). As the Mg is further converted to Mg^{2+} at higher potentials (magenta), removal of the tensile stress from MgO_x will be evidenced as compressive-going Δstress. Interestingly, the surface stress response exhibits a reversible behavior (Figures 1 and S3), even though the Coulombic efficiency is lower than 100% in most cases. This implies that the further oxidation of MgO_x to Mg^{2+} could be happening via a chemical reaction, rather than an electrochemical reaction.

The Δstress(magenta)/Δstress(blue) ratio of $Mg(BH_4)_2$+$LiBH_4$ electrolyte is the highest among the four electrolytes (0.58), while the Coulombic efficiency is the lowest (78.8%). This inconsistent behavior can be attributed to the co-deposition and alloy formation of Mg and Li.[46] We note an additional peak in the surface stress response observed during stripping in the magenta region (Figure 3d) likely reflects the de-alloying process. The production of sharp tensile stress due to dealloying during electrochemical metal deposition processes has been previously described.[72,73]

Last stage of stripping.—One of the most interesting features observed in stripping is the presence of the sharp tensile Δstress (green region) seen just prior to the end of stripping. The magnitude of this feature appears to be electrolyte- and substrate-independent, and is found to be ∼0.85 N/m (Tables S1 and S3). In addition, the magnitude only weakly varies with the scan rate (not shown). Moreover, in Figure S2b, it can be seen that the magnitude of this end-of-stripping tensile Δstress decreases as the negative sweep limit becomes more positive.

The origin of this behavior can be attributed to the strong interaction between Mg and the substrate noble metal atoms (Pt, Au, and Pd). In particular, the calculated E_{ads} of Mg_{ads} is greater on the Pt(111) surface than that on the Mg(0001) surface. Additionally, the calculated Δσ of Mg_{ads} shows a more compressive value on the Pt substrate (Table II). Thus, the Mg layer directly bound to the substrate is oxidized at the end of the stripping process, creating a sharp tensile Δstress.

The overall mechanism of Mg deposition and stripping is shown in Figure 6.

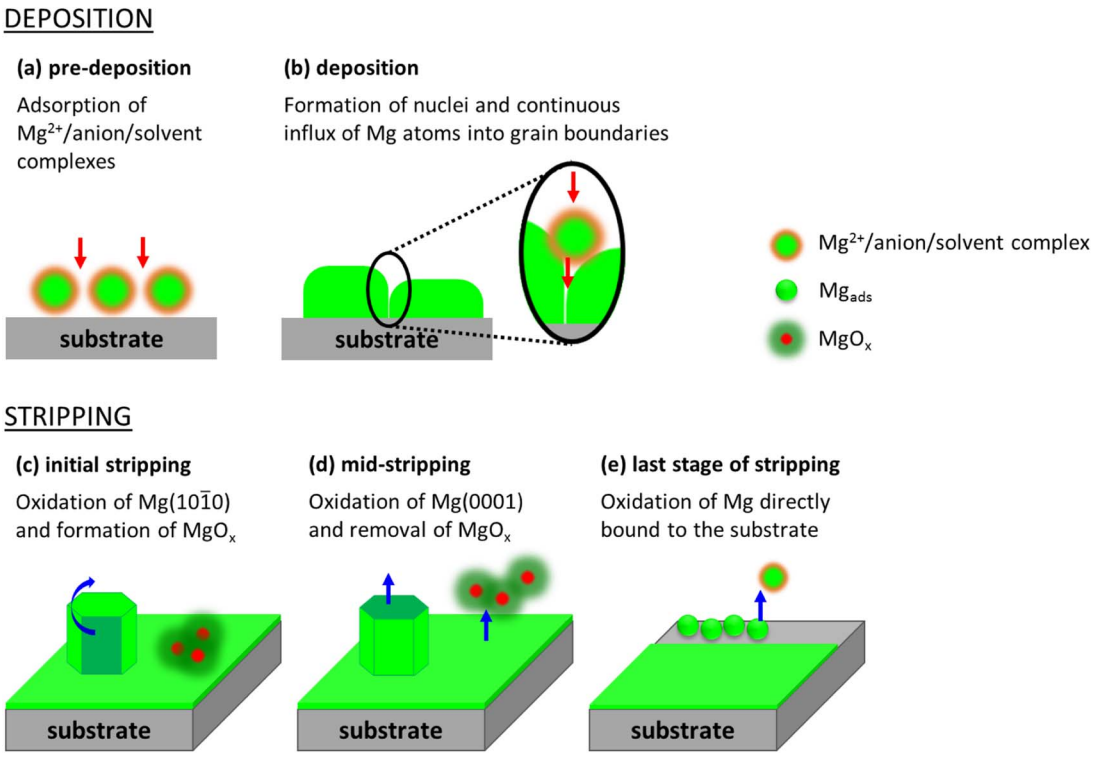

Figure 6. Proposed Mg deposition and stripping scheme.

Conclusions

Surface stress measurements during electrodeposition and stripping of Mg in four different Mg battery electrolytes ($PhMgCl+AlCl_3$/THF, (DTBP)MgCl–$MgCl_2$/THF, $MgCl_2+AlCl_3$/THF, and $Mg(BH_4)_2+LiBH_4$/diglyme) show common features, and each part of the stress-potential curve can be assigned to discrete processes in the deposition and stripping reactions (Figure 6). First, Mg^{2+}/anion/solvent complexes adsorb on the substrate surface prior to the deposition, creating a slight compressive Δstress. As Mg starts to deposit, the surface stress becomes further compressive with a constant stress-film thickness slope, due to formation of nuclei and the absence of recrystallization. During the Mg stripping process, while the removal of Mg contributes a tensile Δstress throughout the stripping process, three distinct Δstress features are observed due to the effect of different Mg crystal planes and the presence of MgO_x. Higher reactivity of the $Mg(10\bar{1}0)$ surface toward anodic dissolution and/or passive oxidation, and more tensile intrinsic surface stress of the Mg(0001) surface create a steep tensile Δstress in the beginning of the stripping, followed by a compressive-going Δstress. Further, formation of MgO_x, which is chemically removed from the surface as the oxidation further proceeds, also contributes to the tensile-to-compressive Δstress during the stripping. Finally, the Mg layer directly bound to the substrate is oxidized at the last step of the stripping, due to the strong interaction between Mg and substrate noble metal atoms (Pt, Au, and Pd).

This study suggests that the active species in the electrolyte act as the same vehicle during the Mg deposition and stripping processes and the reversible Mg electrodeposition/stripping follow general processes as described above. Focusing on these common elements will benefit developing Mg battery electrolytes.

Acknowledgment

Y.H. acknowledges a MWRC Scholarship from the Korean American Scholarship Foundation. This work was supported as part of the Joint Center for Energy Storage Research, an Energy Innovation Hub funded by the U.S. Department of Energy, Office of Science, Basic Energy Sciences. J.G. acknowledges a Department of Energy Early Career award through the Office of Science, Office of Basic Energy Sciences, Chemical, Biological, and Geosciences Division.

References

1. J. Muldoon, C. B. Bucur, A. G. Oliver, T. Sugimoto, M. Matsui, H. S. Kim, G. D. Allred, J. Zajicek, and Y. Kotani, *Energy Environ. Sci.*, **5**, 5941 (2012).
2. H. D. Yoo, I. Shterenberg, Y. Gofer, G. Gershinsky, N. Pour, and D. Aurbach, *Energy Environ. Sci.*, **6**, 2265 (2013).
3. G. Vardar, A. E. S. Sleightholme, J. Naruse, H. Hiramatsu, D. J. Siegel, and C. W. Monroe, *ACS Appl. Mater. Interfaces*, **6**, 18033 (2014).
4. L. W. Gaddum and H. E. French, *J. Am. Chem. Soc.*, **49**, 1295 (1927).
5. J. H. Connor, W. E. Reid Jr., and G. B. Wood, *J. Electrochem. Soc.*, **104**, 38 (1957).
6. T. D. Gregory, R. J. Hoffman, and R. C. Winterton, *J. Electrochem. Soc.*, **137**, 775 (1990).
7. D. Aurbach, Z. Lu, A. Schechter, Y. Gofer, H. Gizbar, R. Turgeman, Y. Cohen, M. Moshkovich, and E. Levi, *Nature*, **407**, 724 (2000).
8. R. E. Doe, R. Han, J. Hwang, A. J. Gmitter, I. Shterenberg, H. D. Yoo, N. Pour, and D. Aurbach, *Chem. Commun.*, **50**, 243 (2014).
9. T. Liu, Y. Shao, G. Li, M. Gu, J. Hu, S. Xu, Z. Nie, X. Chen, C. Wang, and J. Liu, *J. Mater. Chem. A*, **2**, 3430 (2014).
10. R. Mohtadi, M. Matsui, T. S. Arthur, and S.-J. Hwang, *Angew. Chem., Int. Ed.*, **51**, 9780 (2012).
11. Y. Shao, T. Liu, G. Li, M. Gu, Z. Nie, M. Engelhard, J. Xiao, D. Lv, C. Wang, J.-G. Zhang, and J. Liu, *Sci. Rep.*, **3**, 3130 (2013).
12. B. Pan, J. Zhang, J. Huang, J. T. Vaughey, L. Zhang, S.-D. Han, A. K. Burrell, Z. Zhang, and C. Liao, *Chem. Commun.*, **51**, 6214 (2015).
13. O. Mizrahi, N. Amir, E. Pollak, O. Chusid, V. Marks, H. Gottlieb, L. Larush, E. Zinigrad, and D. Aurbach, *J. Electrochem. Soc.*, **155**, A103 (2008).
14. W. Haiss, *Rep. Prog. Phys.*, **64**, 591 (2001).
15. T. S. Arthur, P.-A. Glans, M. Matsui, R. Zhang, B. Ma, and J. Guo, *Electrochem. Cummun.*, **24**, 43 (2012).
16. J. L. Esbenshade, C. J. Barile, T. T. Fister, K. L. Bassett, P. Fenter, R. G. Nuzzo, and A. A. Gewirth, *J. Phys. Chem. C*, **119**, 23366 (2015).
17. J. A. Venables, G. D. T. Spiller, and M. Hanbuecken, *Rep. Prog. Phys.*, **47**, 399 (1984).
18. R. Koch, *J. Phys. Condens. Matter*, **6**, 9519 (1994).
19. J. A. Floro, S. J. Hearne, J. A. Hunter, P. Kotula, E. Chason, S. C. Seel, and C. V. Thompson, *J. Appl. Phys.*, **89**, 4886 (2001).
20. O. E. Kongstein, U. Bertocci, and G. R. Stafford, *J. Electrochem. Soc.*, **152**, C1163 (2005).
21. M. J. Chon, V. A. Sethuraman, A. McCormick, V. Srinivasan, and P. R. Guduru, *Phys. Rev. Lett.*, **107**, 045503 (2011).
22. S. K. Soni, B. W. Sheldon, X. Xiao, and A. Tokranov, *Scr. Mater.*, **64**, 307 (2011).
23. A. Mukhopadhyay, A. Tokranov, X. Xiao, and B. W. Sheldon, *Electrochim. Acta*, **66**, 28 (2012).
24. V. A. Sethuraman, N. Van Winkle, D. P. Abraham, A. F. Bower, and P. R. Guduru, *J. Power Sources*, **206**, 334 (2012).
25. H. Tavassol, M. K. Y. Chan, M. G. Catarello, J. Greeley, D. G. Cahill, and A. A. Gewirth, *J. Electrochem. Soc.*, **160**, A888 (2013).
26. H. Tavassol, M. W. Cason, R. G. Nuzzo, and A. A. Gewirth, *Adv. Energy Mater.*, **5**, 1400317 (2015).
27. J.-Y. Go and S.-I. Pyun, *J. Electrochem. Soc.*, **150**, A1037 (2003).
28. S.-I. Pyun, J.-Y. Go, and T.-S. Jang, *Electrochim. Acta*, **49**, 4477 (2004).
29. K. Y. Chung and K.-B. Kim, *J. Electrochem. Soc.*, **149**, A79 (2002).
30. C. J. Barile, E. C. Barile, K. R. Zavadil, R. G. Nuzzo, and A. A. Gewirth, *J. Phys. Chem. C*, **118**, 27623 (2014).
31. J. L. Langer, J. Economy, and D. G. Cahill, *Macromolecules*, **45**, 3205 (2012).
32. P. E. Bloechl, *Phys. Rev. B*, **50**, 17953 (1994).
33. G. Kresse and D. Joubert, *Phys. Rev. B*, **59**, 1758 (1999).
34. M. Marsman and G. Kresse, *J. Chem. Phys.*, **125**, 104101 (2006).
35. J. P. Perdew, K. Burke, and M. Ernzerhof, *Phys. Rev. Lett.*, **77**, 3865 (1996).
36. G. Kresse and J. Hafner, *Phys. Rev. B*, **48**, 13115 (1993).
37. G. Kresse and J. Furthmueller, *Phys. Rev. B*, **54**, 11169 (1996).
38. H. J. Monkhorst and J. D. Pack, *Phys. Rev. B*, **13**, 5188 (1976).
39. G. Raynor and W. H. Rothery, *J. Inst. Metals*, **65**, 379 (1939).
40. D. R. Lide, *CRC Handbook of Chemistry and Physics, 78th Edition*, CRC Press (1997).
41. C. Kittel, *Introduction to Solid State Physics, 4th Ed*, Wiley (1971).
42. J. Zhang, D. W. Zhou, L. P. He, P. Peng, and J. S. Liu, *J. Phys. Chem. Solids*, **70**, 32 (2009).
43. T. Bredow and A. R. Gerson, *Phys. Rev. B*, **61**, 5194 (2000).
44. Z.-H. Zeng, J. L. F. Da Silva, H.-Q. Deng, and W.-X. Li, *Phys. Rev. B*, **79**, 205413 (2009).
45. Y. Ha, Z. Zeng, Y. Cohen, J. Greeley, and A. A. Gewirth, *J. Phys. Chem. C*, **120**, 8674 (2016).
46. J. Chang, R. T. Haasch, J. Kim, T. Spila, P. V. Braun, A. A. Gewirth, and R. G. Nuzzo, *ACS Appl. Mater. Interfaces*, **7**, 2494 (2015).
47. M. Matsui, *J. Power Sources*, **196**, 7048 (2011).
48. D. J. Wetzel, M. A. Malone, R. T. Haasch, Y. Meng, H. Vieker, N. T. Hahn, A. Gölzhäuser, J.-M. Zuo, K. R. Zavadil, A. A. Gewirth, and R. G. Nuzzo, *ACS Appl. Mater. Interfaces*, **7**, 18406 (2015).
49. K. A. See, K. W. Chapman, L. Zhu, K. M. Wiaderek, O. J. Borkiewicz, C. J. Barile, P. J. Chupas, and A. A. Gewirth, *J. Am. Chem. Soc.*, **138**, 328 (2016).
50. M. Liu, Y. Han, L. Tang, J.-F. Jia, Q.-K. Xue, and F. Liu, *Phys. Rev. B*, **86**, 125427 (2012).
51. L. Vitos, A. V. Ruban, H. L. Skriver, and J. Kollar, *Surf. Sci.*, **411**, 186 (1998).
52. H. Ibach, *Surf. Sci. Rep.*, **29**, 193 (1997).
53. M. W. Chase, *NIST-JANAF Thermochemical Tables. 4th Edition*, American Chemical Society (1998).
54. C. Kittel, *Introduction to Solid State Physics*, Wiley (2005).
55. E. Kaxiras, *Atomic and Electronic Structure of Solids*, Cambridge University Press (2003).
56. A. Benmayza, M. Ramanathan, T. S. Arthur, M. Matsui, F. Mizuno, J. Guo, P.-A. Glans, and J. Prakash, *J. Phys. Chem. C*, **117**, 26881 (2013).
57. R. C. Cammarata, T. M. Trimble, and D. J. Srolovitz, *J. Mater. Res.*, **15**, 2468 (2000).
58. C. Friesen, S. C. Seel, and C. V. Thompson, *J. Appl. Phys.*, **95**, 1011 (2004).
59. W. Haiss, R. J. Nichols, and J.-K. Sass, *Surf. Sci.*, **388**, 141 (1997).
60. J. W. Shin, C. Hangarter, U. Bertocci, Y. Liu, T. P. Moffat, and G. R. Stafford, *J. Electrochem. Soc.*, **159**, D479 (2012).
61. D. Aurbach, A. Schechter, M. Moshkovich, and Y. Cohen, *J. Electrochem. Soc.*, **148**, A1004 (2001).
62. A. Bhandari, S. J. Hearne, B. W. Sheldon, and S. K. Soni, *J. Electrochem. Soc.*, **156**, D279 (2009).
63. E. Chason, *Thin Solid Films*, **526**, 1 (2012).
64. H. Z. Yu and C. V. Thompson, *Acta Mater.*, **67**, 189 (2014).
65. D. Magnfält, A. Fillon, R. D. Boyd, U. Helmersson, K. Sarakinos, and G. Abadias, *J. Appl. Phys.*, **119**, 055305 (2016).
66. M. Liu, D. Qiu, M.-C. Zhao, G. Song, and A. Atrens, *Scr. Mater.*, **58**, 421 (2007).
67. C. R. McCall, M. A. Hill, and R. S. Lillard, *Corros. Eng., Sci. Technol.*, **40**, 337 (2005).
68. G.-L. Song and Z. Xu, *Corros. Sci.*, **63** 100 (2012).
69. K. S. Shin, M. Z. Bian, and D. N. Nguyen, *JOM*, **64**, 664 (2012).
70. J. Ghijsen, H. Namba, P. A. Thiry, J. J. Pireaux, and P. Caudano, *Appl. Surf. Sci.*, **8**, 397 (1981).
71. P. A. Thiry, J. Ghijsen, R. Sporken, J. J. Pireaux, R. L. Johnson, and R. Caudano, *Phys. Rev. B*, **39**, 3620 (1989).
72. J. W. Shin, U. Bertocci, and G. R. Stafford, *J. Phys. Chem. C*, **114**, 7926 (2010).
73. J. W. Shin, U. Bertocci, and G. R. Stafford, *J. Phys. Chem. C*, **114**, 17621 (2010).